Available online at www.sciencedirect.com

jmr&t Journal of Materials Research and Technology

journal homepage: www.elsevier.com/locate/jmrt

Microstructure evolution and deformation mechanisms during compression of a harmonic–structured Ti–24Nb–4Zr–8Sn alloy

Benoît Fer [a,d,**], *David Tingaud* [a], *Jenő Gubicza* [b,*], *Nguyen Quang Chinh* [b], *Yulin Hao* [c], *Fabien Cazes* [a], *Frédéric Prima* [d], *Guy Dirras* [a]

[a] *Université Sorbonne Paris Nord, Laboratoire de Sciences des Procédés et des Matériaux, CNRS, UPR 3407, 93430 Villetaneuse, France*

[b] *Department of Materials Physics, Eötvös Loránd University, Budapest, POB 32, H-1518, Hungary*

[c] *Shi-Changxu Innovation Center for Advanced Materials, Institute of Metal Research, Chinese Academy of Sciences, Shenyang 110016, China*

[d] *PSL University, Chimie ParisTech, CNRS, Institut de Recherche de Chimie Paris, Paris 75005, France*

ARTICLE INFO

Article history:
Received 5 July 2023
Accepted 28 July 2023
Available online 2 August 2023

Keywords:
Titanium alloy
Harmonic structure
Spark Plasma Sintering
Dislocations
Plasticity mechanisms
Hetero-deformation induced stress

ABSTRACT

Processing heterogeneous microstructures, especially the so-called harmonic structures consisting of soft core and hard shell regions, is an efficient way to achieve a strength-ductility trade-off in classical metallurgy. In this study, two harmonic samples with the same composition of Ti–24Nb–4Zr–8Sn but different microstructures were processed to exhibit different grain size heterogeneities between the core and the shell. Both samples were consolidated from a ball-milled powder using Spark Plasma Sintering (SPS) but applying two different sintering times, 1 and 60 min. The grain size heterogeneities were higher for the longer SPS sintering time due to the enhanced grain dimension in the core for 60 min consolidation time. The mechanical behavior of the two materials was studied via a monotonic quasi-static compression test. For both harmonic-structured Ti–24Nb–4Zr–8Sn alloys, a high compressive proof stress of about 1 GPa was detected. The strain-hardening rate was higher for the longer SPS time due to the higher grain size differences between the core and shell. A high dislocation density was detected in both materials after compression deformation (several tens of 10^{14} m^{-2}). The dislocations tend to form cells and LAGBs during compression. The dislocation pile-ups at the core-shell interfaces caused a back stress of about 640 MPa after compression at 2–5% strains. The contributions of the different features of the microstructure (grain size, α phase precipitates, and oxygen concentration) to the proof stress were determined.

* Corresponding author. Department of Materials Physics, Eötvös Loránd University, Budapest, POB 32, H-1518, Hungary.
** Corresponding author.
E-mail addresses: ferbenoit@gmail.com (B. Fer), jeno.gubicza@ttk.elte.hu (J. Gubicza).

https://doi.org/10.1016/j.jmrt.2023.07.250

1. Introduction

In order to achieve a compromise between strength and ductility of metallic alloys [1], materials with heterogeneous structures have been proposed as possible solutions over the past years. Processing routes were first based on Severe Plastic Deformation (SPD) – local or global – eventually followed by a recrystallization heat treatment [2–4]. However, Powder Metallurgy (PM) route is also a viable alternative to fabricate such microstructures [5,6].

Among PM processing routes, the harmonic structure design concept has been simultaneously developed through two distinct processing routes by Vajpai et al. [7] and Dirras et al. [8]. The former processing route combines both SPD through ball milling (BM) of spherical and pre-alloyed powder particles and sintering, whereas the latter one is based on blending and sintering of nano-grained and coarse-grained powders with controlled volume fractions. Nevertheless, the two experimental methodologies result in similar microstructures, consisting of an interconnected three-dimensional network of fine-grained areas (the shell) surrounding coarse-grained areas (the core). Such a microstructure has been experimented for many materials, including steel [9,10], Co–Cr-based alloys [11], Ni alloys [8], commercially pure (CP) titanium [12], α/β titanium alloys [12,13], and more recently on β-type titanium alloys. Furthermore, on top of grain size heterogeneities, chemical heterogeneities between core and shell may also exist in harmonic-structured materials. More details on harmonic-structured materials can be found in [14].

The main idea of designing harmonic-structured materials is to improve the strength-ductility synergy. Indeed, a significant increase in strength has been noticed for harmonic-structured steel [9], which could be understood by the commonly accepted deformation mechanisms in heterogeneously structured materials. Grain size heterogeneities and, or precipitates, induce local hardness heterogeneities in the material. Consequently, plastic deformation does not start simultaneously in the whole material; plastic deformation in soft areas starts earlier than in hard areas. Therefore, strain heterogeneities are created in the material during plastic deformation. A network of Geometrically Necessary Dislocations (GNDs) must accommodate these deformation incompatibilities to avoid initiating and propagating the damage in the material [14,15]. GNDs are thus created; they pile up at the hard/soft interfaces, and induce high back stress in the material, contributing to the overall hardening of the material through kinematic work hardening [16–18]. The effect of GNDs on work hardening has been recently renamed hetero-deformation-induced (HDI) strain hardening [19]. Indeed, back stresses are created by the accumulation of dislocations on the interfaces between hard and soft domains. This type of stress is always directional and acts against the propagation of newly formed dislocations in the soft domains. However, forward stress is also created in hard domains at the top of pile-ups, acting opposite to back stress. Consequently, hard domains are also affected by dislocation pile-ups [20].

However, uncertainties remain concerning the origin of GNDs. Some studies argue that they are first emitted in soft domains by Frank-Read sources or grain boundaries and then propagate in the microstructure until they reach the hard/soft interfaces. Frank-Read sources could be dynamically activated by pinning jogs between two gliding dislocations and quickly afterward deactivated by a new jog of dislocations. As the strain increases, dislocation sources near the shell are also progressively activated [21]. However, others argue that they could be emitted and trapped directly at the interfaces, where the density of structural defects, which are potential Frank-Read sources, is higher [22]. Nevertheless, the importance of hardening gradients at the interfaces in uncovering deformation mechanisms of heterogeneously structured materials is evident [23].

A Ti–24Nb–4Zr–8Sn alloy with a harmonic microstructure will be studied in this work. This alloy belongs to the β-metastable titanium alloy family. Therefore, it has a high potential for biomedical applications. This is due, on the one hand, to the low Young's modulus of the alloy (about 40–50 GPa) and, on the other hand, to the absence of cytotoxic elements in its chemical composition [24]. However, yield and fatigue strength are still to be improved [25], and the design of harmonic structures aims to improve these properties.

In harmonic-structured Ti–24Nb–4Zr–8Sn alloy, deformation mechanisms of heterogeneous materials could occur together with complex deformation mechanisms such as transformation-induced plasticity (TRIP) and/or twinning-induced plasticity (TWIP). Conventional Ti–24Nb–4Zr–8Sn alloy has indeed been proved to show martensitic phase transformation of the parent bcc β phase to orthorhombic α'' phase during straining [26–28]. Moreover, intense mechanical twinning sometimes occurs depending on the mechanical solicitation mode of Ti–24Nb–4Zr–8Sn alloy. Some authors argue that the primary twinning mode is $\{332\}\langle 113\rangle_{\beta}$ [29]. The orientation of these types of twins could be linked with martensitic phase transformation; $\{332\}\langle 113\rangle_{\beta}$ twins might be the traces of $\{130\}\langle 310\rangle_{\alpha''}$ twins, which have been formed in α'' phase before it is reversed. Traces of α'' martensite are, in this case, found near twin boundaries. However, in other studies, the main twinning mode remains the bcc-conventional $\{112\}\langle 111\rangle_{\beta}$ one [30], and the interfacial ω phase is sometimes formed at the twin boundaries [31].

This study investigates the hardening mechanisms of a Ti–24Nb–4Zr–8Sn alloy with harmonic structure by studying the compression behavior of two harmonic samples with different microstructural features processed from powder with different sintering times. A focus is made on grain size heterogeneities between the core and the shell by studying two samples with differences in grain sizes between the core and the shell. Yet, the role of other microstructural features, like α phase volume fraction and oxygen content, will also be considered in the discussion. Different experimental methods analyze the evolution of the microstructure during compression and aim to distinguish some of the hardening mechanisms, including the efficiency of boundaries between heterogeneous domains to generate GND pile-ups and HDI stress concentrations inside the material.

2. Materials and methods

Harmonic-structured Ti–24Nb–4Zr–8Sn samples were processed via PM route. Spherical and pre-alloyed powder

particles, which have been argon atomized at the Institute of Metal Research (IMR) from the Chinese Academy of Sciences, were used as raw materials for this work. The initial particle diameter was between 100 and 160 μm. BM was performed using a Retsch PM 100 planetary ball mill under the following conditions: ball-to-powder ratio (BPR) of 2:1, a rotational speed of 200 rpm, milling time of 50 h, steel materials for bowl and balls, and argon atmosphere. Spark Plasma Sintering (SPS) was applied for powder consolidation using Dr. Sinter 515 S Syntex setup belonging to the "Plateforme de Frittage Île-de-France" (Thiais, France), with the following parameters: temperature of 800 °C, pressure of 100 MPa, heating rate of 50 °C/min and argon atmosphere. The only difference in the processing parameters of the two samples was the SPS holding time. Two different holding times of 1 min and 60 min were selected for SPS processing of the samples; therefore, they are respectively denoted as "SPS − 1 min" and "SPS − 60 min" in this study.

For the mechanical characterization, compression tests were performed using a Deben micro-machine (maximum load of 5 kN) on samples with the dimensions of 2 mm × 2 mm x 3 mm. These specimens were prepared from SPS-processed cylindrical billets with a diameter of 8 mm in transverse direction using Electron Discharge Machining. The compression machine was operated under displacement control, leading to a constant strain rate of 10^{-3} s^{-1}. Digital Image Correlation was used for extensometry purposes only, to obtain accurate strain measurements on the samples. To this end, a black and white fleck was made on the samples with an aerograph before compression tests. Pictures of the samples were then acquired during the deformation using an Allied Vision camera at a frequency of 2 images/s. The strain was then determined directly by measuring the evolution of the length of a segment on the surface of the samples. Loading-unloading-reloading compression tests were also performed at the strain values of 2% and 5%. At each strain, the microstructure was investigated after unloading and the back stress was determined using the method given in section 4.

X-ray diffraction (XRD) measurements were acquired for the determination of the phase composition using a Smartlab diffractometer (manufacturer: Rigaku, Japan), using a CuKα X-ray radiation (wavelength: λ = 0.15418 nm) and a 2 mm square diaphragm, working in Bragg-Brentano geometry. X-ray Line Profile Analysis (XLPA) was performed on the diffractograms acquired by a high-resolution rotating anode diffractometer (type: RA-MultiMax9, manufacturer: Rigaku, Japan) using CuKα_1 radiation (wavelength λ = 0.15406 nm). The height and the width of the rectangular X-ray spot on the sample surface were 1.5 and 0.2 mm, respectively. The measured peak profiles of the main bcc β-phase were evaluated by the Convolutional

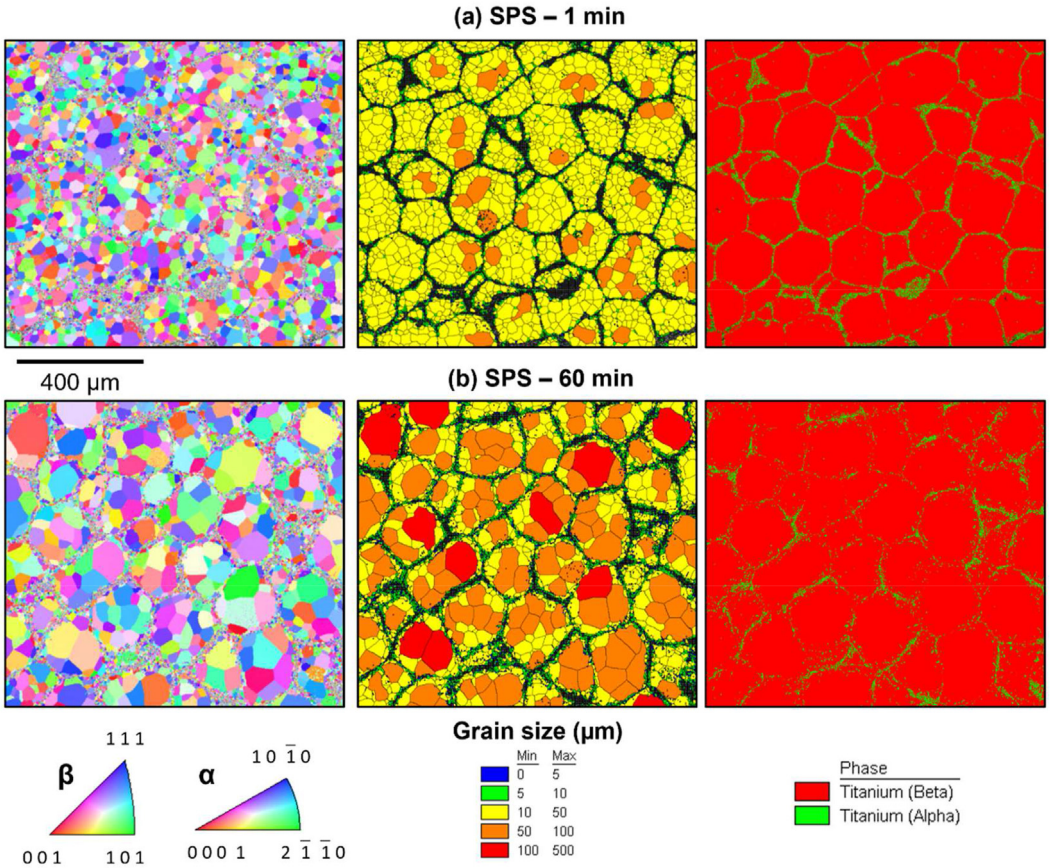

Fig. 1 − Microstructural characterization of the two initial harmonic Ti−24Nb−4Zr−8Sn samples SPS − 1 min (a) and SPS − 60 min (b). From left to right: IPF maps, grain size, and phase maps of a 1 mm² area obtained by EBSD with a step size of 1.5 μm.

Multiple Whole Profile (CMWP) fitting procedure [32]. In this method, the diffraction pattern is fitted by the sum of a background spline, and the diffraction peaks are obtained as the convolution of the theoretical line profiles related to crystallite size and dislocations. The CMWP fitting gives the area-weighted mean crystallite size ($<x>_{area}$), the dislocation density (ρ), parameter q describing the edge/screw character of dislocations, and the dislocation arrangement parameter (M). The more shielded the strain field of dislocations (e.g., when the dislocations are arranged into low-angle grain boundaries (LAGBs) or dipolar walls), the lower the value of the latter quantity.

Scanning Electron Microscopy (SEM) and Electron Backscatter Diffraction (EBSD) experiments were performed using a ZEISS SUPRA 40VP scanning electron microscope equipped with a field emission gun and an EBSD acquisition system. Depending on the resolution needed, a step size of 0.25 μm or 1.5 μm was used. EBSD data collection was performed with a NORDIF camera, and the data treatment was carried out using TSL OIM software. The Kernel Average Misorientation (KAM) parameter was calculated for each pixel by considering misorientations with the three first neighbors. Nanoindentation measurements were performed using a UMIS indentation device with a Berkovich indenter and applying a maximum load of 5 mN. A few hundred indentations were carried out along a straight line, with a step size of 10 μm, which is superior to four times the dimension of the indentation pattern.

3. Results

3.1. *Microstructural and mechanical characterizations of the initial samples*

The microstructures of samples SPS – 1 min and SPS – 60 min are shown in Fig. 1. They were processed by a PM route combining BM and SPS as described in section 2 and reference [33]. The evolution of the morphology and the microstructure of the powder particles during BM is illustrated in Supplementary S1. The highly deformed crown on the surface of the powder particles (which is visible on Figs S1-1 and S1-2) recrystallizes during SPS to create the shell of the structure. The microstructures thus comprise a 3D network of fine-grained dual-phase domains containing α and β phases and a coarse-grained β component called as "shell" and "core", respectively.

The main microstructural features of the samples are listed in Table 1. The processing route of the two samples is very similar. As a result, they exhibit comparable values of shell fraction (about 25%) and α phase fraction (about 8%). However, slight differences in α phase volume fraction between the samples are highlighted by EBSD analysis and confirmed by XRD measurements. The holding time of SPS has been proven to influence grain growth during consolidation [34]: the longer the SPS holding time, the coarser the microstructure. In the case of the present harmonic structures, the size of grains in the shell did not vary considerably with holding time during SPS; conversely, the grain size in the core increased from 33 to 62 μm when the SPS holding time was enhanced from 1 to 60 min. As a result, the grain size heterogeneity is higher in the material processed with a longer holding time during SPS. The grain size differences can be estimated using the R ratio, defined as the average size of the grains in the core divided by the average size of the grains in the shell:

$$R = \frac{d_{core}}{d_{shell}}, \quad (1)$$

where d_{core} and d_{shell} represent the average grain sizes in the core and the shell, respectively. The values of R ratio were about 9.2 and 18.5 for samples SPS – 1 min and SPS - 60 min, respectively. This microstructural parameter is expected to have an impact on the mechanical behavior.

The microstructural heterogeneity associated with the core-shell structure is supposed to result in local hardness heterogeneities. Nanoindentation measurements were performed on samples SPS – 1 min and SPS – 60 min to check the mechanical inhomogeneity, and the obtained nanohardness distributions and profiles for the two specimens are displayed in Fig. 2. The average hardness value was equal to 10.2 GPa for specimen SPS – 1 min and 8.0 GPa for sample SPS – 60 min. For specimen SPS – 1 min, most of the hardness values are between 6 and 11 GPa; however, there are much higher values ranging from 13 to 35 GPa (see Fig. 2(a)). These values correspond to the shell, which is significantly harder than the core. It is also confirmed by the 1200 μm long hardness profiles of both samples (see Fig. 2 (b)), where we can see that the distance between two successive hardness peaks is about 150 μm. This value is like the typical spacing between the shells in the investigated harmonic microstructures (see Fig. 1). Due to the much higher hardness of the shell region, an asymmetric hardness distribution was observed for both samples. It is noted that the hardness values were lower for sample SPS – 60 min than for specimen SPS - 1 min. For instance, the highest hardness values for sample SPS - 60 min were about 15 GPa, while they were above 20 GPa for specimen SPS – 1 min.

The higher hardness of the shell can be attributed at least partly to the smaller grain size. In addition, a former study revealed that the phase composition heterogeneities – i.e., the presence of both β and α phases in the shell while the core has a complete β structure –and a probable, solid solution hardening due to the local increase of oxygen concentration in the

Table 1 – Microstructural features of the two studied samples as obtained by EBSD. The notations * and ** indicate that EBSD was performed on a 1 mm² area with a step size of 1.5 μm and a 400 μm² zone with a step size of 0.25 μm, respectively.

Processing parameters	Average grain size (μm) *	Grain size in the core (μm) *	Grain size in the shell (μm) **	Ratio R *	Shell fraction (%) **	α phase fraction (%) **
SPS time: 1 min	30	33	3.6	9.2	22	8
SPS time: 60 min	54	62	3.4	18.5	26	10

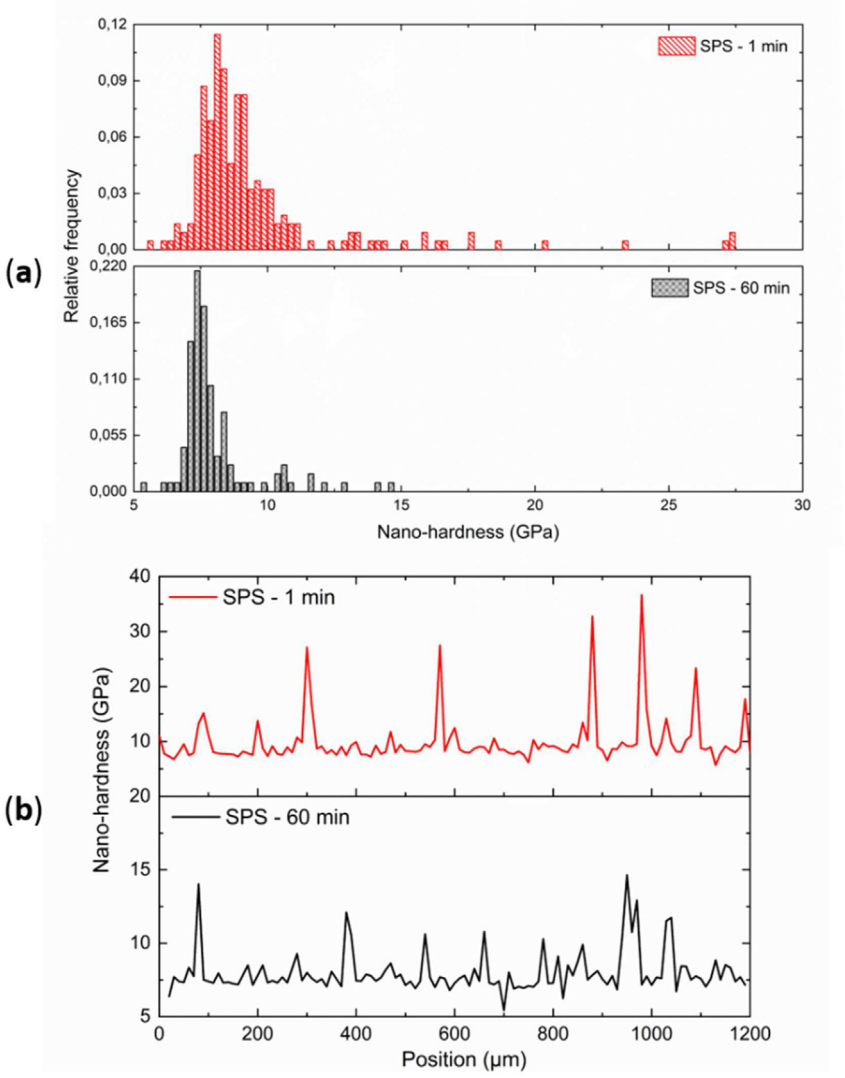

Fig. 2 – (a) Nanohardness distributions for both samples SPS – 1 min (top, in red) and SPS – 60 min (bottom, in black). (b) Spatial distribution of nanohardness along a 1200 μm long line on the specimen surfaces.

shell could also contribute to the high hardness of the shell [35]. Oxygen is an α-stabilizer element; therefore, its higher concentration in the shell can contribute to the significant fraction of α phase in that region [36]. Furthermore, the deformability of the α phase is low at room temperature due to its hexagonal close-packed (hcp) structure which also hardens the shell. The local oxygen enrichment in the shell has been analyzed in a previous study [33] by Wavelength Dispersion Spectroscopy (WDS) investigations, and the oxygen repartition map clearly showed an increase in oxygen concentration within the shell. For example, the oxygen map for a harmonic-structured Ti–24Nb–4Zr–8Sn sample SPS-processed for 30 min is available in supplementary Fig. S2 of this work and our previous paper [33]. The oxygen enrichment of the samples occurred during BM. It has already been shown that oxygen and α phase strengthening effects can cause significant hardening in titanium alloys [37,38]. It should be noted that during SPS, oxygen may diffuse from the shell to the core due to the high temperature of sintering. The longer sintering time for sample SPS – 60 min compared to specimen SPS – 1 min may result in a smaller oxygen concentration in the shell, yielding a lower hardening effect.

Compression tests were performed on SPS – 1 min and SPS – 60 min samples to evaluate the effect of the different microstructures on the mechanical behavior of the harmonic-structured Ti–24Nb–4Zr–8Sn alloys. The compression curves for both SPS – 1 min and SPS - 60 min samples are shown in Fig. 3. The two samples reach high compressive yield strengths of about 900 MPa. The compression tests were interrupted before the stress reached the limits of the micro-machine, and consequently, the strain at the end of the compression curve does not correspond to the strain at failure of the samples. Two parallel mechanical tests were performed for each sample. The uncertainty of the stress values determined from the compression curves was about 5% as estimated from the difference between the results obtained from the two tests.

It seems that the more pronounced the grain size gradients in the microstructure – i.e., the higher the R ratio – the higher the strain hardening rate of the sample. Indeed, strain

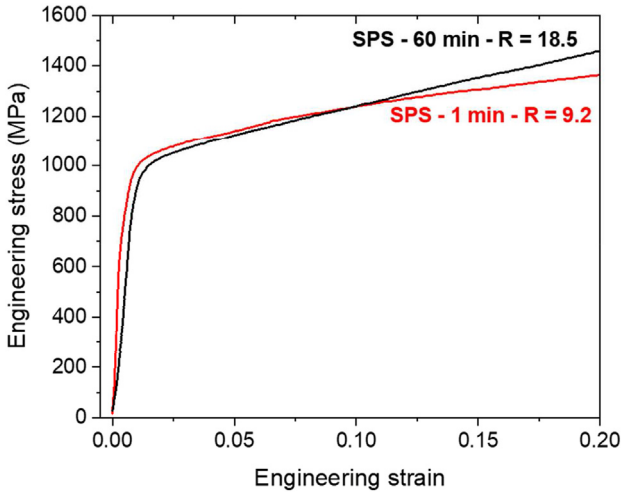

Fig. 3 – Compression curves of harmonic-structured Ti–24Nb–4Zr–8Sn samples: SPS – 1 min (red) and SPS – 60 min (black). The strain rate during the compression tests was 10^{-3} s^{-1}. The values of R indicate the ratio of the grain sizes of the core and shell parts of the microstructures.

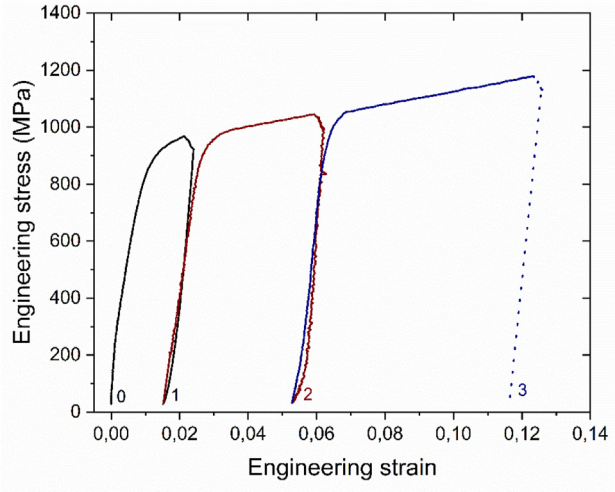

Fig. 4 – Compression curve for sample SPS – 60 min. The numbers indicate the different stages of deformation where the compression test was interrupted for the study of the microstructure. The last part of the curve, indicated by a dotted line, shows an elastic unloading which could not be appropriately recorded; therefore, it was estimated using the elastic modulus of the material.

hardening rate keeps an average value of about 2 GPa for SPS - 60 min at high plastic strains, whereas the average strain hardening rate for SPS – 1 min is only about 1 GPa in the strain range between 0.1 and 0.2. These micro-mechanical test results were completed by a microstructural investigation of the samples at different strain percentages, which is presented in the following paragraphs.

3.2. *Ex-situ study of the microstructure evolution during compression of sample SPS - 60 min*

For a better understanding of the proceeding of plastic deformation for sample SPS – 60 min exhibiting the higher R value, the compression tests were interrupted at different strain values of 2%, 5%, and 12%. The interrupted compression curve is plotted in Fig. 4, and the microstructure was studied at each stage, denoted by the numbers from 0 to 3 in Fig. 4.

Fig. 5 shows SEM backscattered electron micrographs, which were taken on the same area of the sample SPS – 60 min compressed up to different strain values denoted by numbers ranging from 0 to 3 as indicated in Fig. 4. Slip bands appeared on the surface of the sample even at a low plastic strain of 2%. These slip bands are also visible on the Inverse Pole Figure (IPF) maps of Fig. 6. They are mainly formed in the β grains of the core. Both their density and height seem to increase when strain increases in the material. Some grains – especially at high strain values - show bands in different directions which overlap and present shear phenomena at their intersection. This is because 12 gliding systems may be activated for ½ <111> $\{110\}_\beta$ dislocations in bcc crystals. Dislocations with the Burgers vector ½ <111> are also likely to slip on $\{112\}_\beta$ and $\{123\}_\beta$ lattice planes. In our case, at least two or three gliding systems seem to be activated in each grain. Moreover, dislocations can cross-slip from one gliding plane to another, and the high number of slip systems favors this event in the case of bcc alloys. Indeed, in the pictures in Fig. 5, slip bands are straight and sometimes become wavy when strain increases above 2%. Cross-slip between $\{110\}_\beta$ lattice planes is very likely to occur and can explain the wavy shape of the bands. These zigzag features could be attributed to a pencil glide mechanism, usually reported to be active in bcc crystals [39] and even in Mg_2SiO_4 olivine, which has an orthorhombic structure [40]. Indeed, pencil glide has recently been evidenced in a bulk β-Ti21 S (Ti15Mo-2.7Nb–3Al-0.2Sn) polycrystal by Ben Haj Slama et al [41].

Another significant observation is the efficiency of the shell as an obstacle against the plastic flow. Indeed, slip bands are not transmitted from one core-shell structure to its neighboring one. This is clear from the close-up views of core-shell boundaries, which are also presented in Fig. 5.

From the close-up views of the shell vicinity in Fig. 5(d–e), we can also notice slip bands inside small-sized β grains in the shell of the sample SPS – 60 min. However, their amplitude is minimal compared to those in the coarse grains of the core. On the contrary, slip bands are not visible inside α grains; therefore, the efficiency of the shell as an obstacle against plastic flow might be related at least partly to α precipitates. At a low strain value of 2–5%, most of the dislocation slip bands which encounter a precipitate seem to be stopped by the obstacles (see Fig. 5 (d)), whereas, at higher strains, some precipitates are sheared by the slip bands (see Fig. 5 (e)). This may also result in the formation of small cracks in the precipitates and may start damage in the material, as will be described later in section 3.4. Such typical cracks are visible and indicated by red arrows in Fig. 5 (e) for the strain of 15%.

The evolution of the microstructure in sample SPS – 60 min during interrupted compression tests was also studied by EBSD. Fig. 6 shows the EBSD analysis of the microstructure of

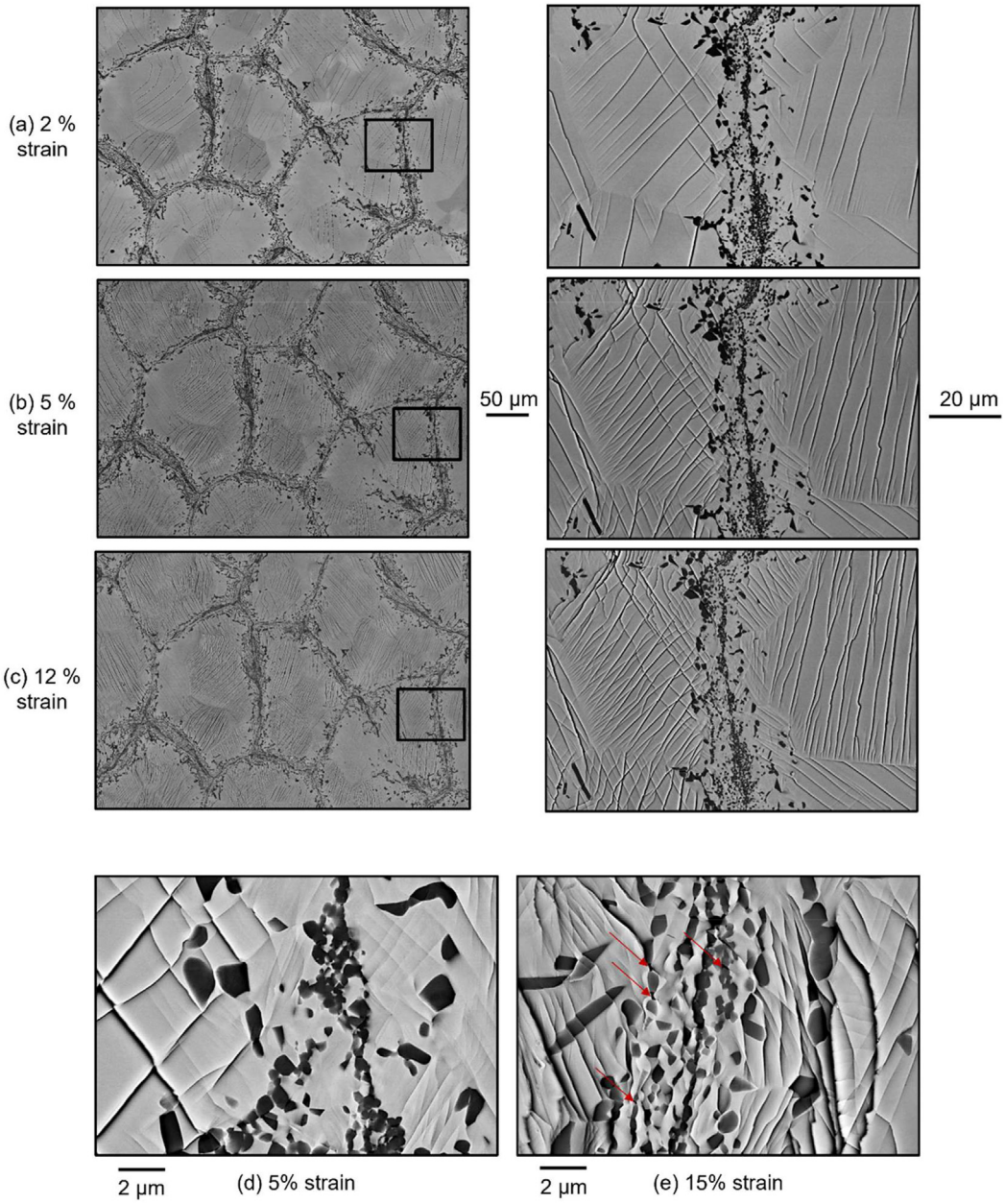

Fig. 5 – Evidence of the formation of slip bands on the surface of harmonic-structured Ti–24Nb–4Zr–8Sn (SPS – 60 min) specimen during compression test. The backscattered electron images were taken on the same area after compression up to the strains of (a) 2%, (b) 5%, and (c) 12%. The areas indicated by the black squares on the images at the left side are shown with higher magnification at the right side. Figures (d–e) present close-up views of core-shell boundaries at strains of 5% (d) and 15% (e) – with cracks indicated with red arrows.

sample SPS – 60 min at different strains of the interrupted compression tests. It must be noted that the analyzed area was the same as that presented in Fig. 5. Both IPF and KAM maps are presented in Fig. 6. Misorientations inside the grains increased, and additionally, LAGBs were created during compression tests. They can be formed due to the clustering of dislocations.

The KAM image is a graphical representation of local average misorientations in the microstructure. In the initial sample, high local misorientations (indicated by the red color in Fig. 6) can be seen in the shell: they are caused by the fine microstructure with α precipitates. When plastic deformation starts, low misorientations appear in the structure of sample SPS – 60 min (indicated by the green color in Fig. 6). This effect is moderate at 2% strain, but more pronounced for 5% compressive strain. Moreover, for strains higher than 5% the highly misorientated volumes can be found mainly in the shell vicinity which is a consequence of the deformation mechanisms occurring in heterogeneous microstructures (e.g., the formation of dislocation slip bands in the vicinity of

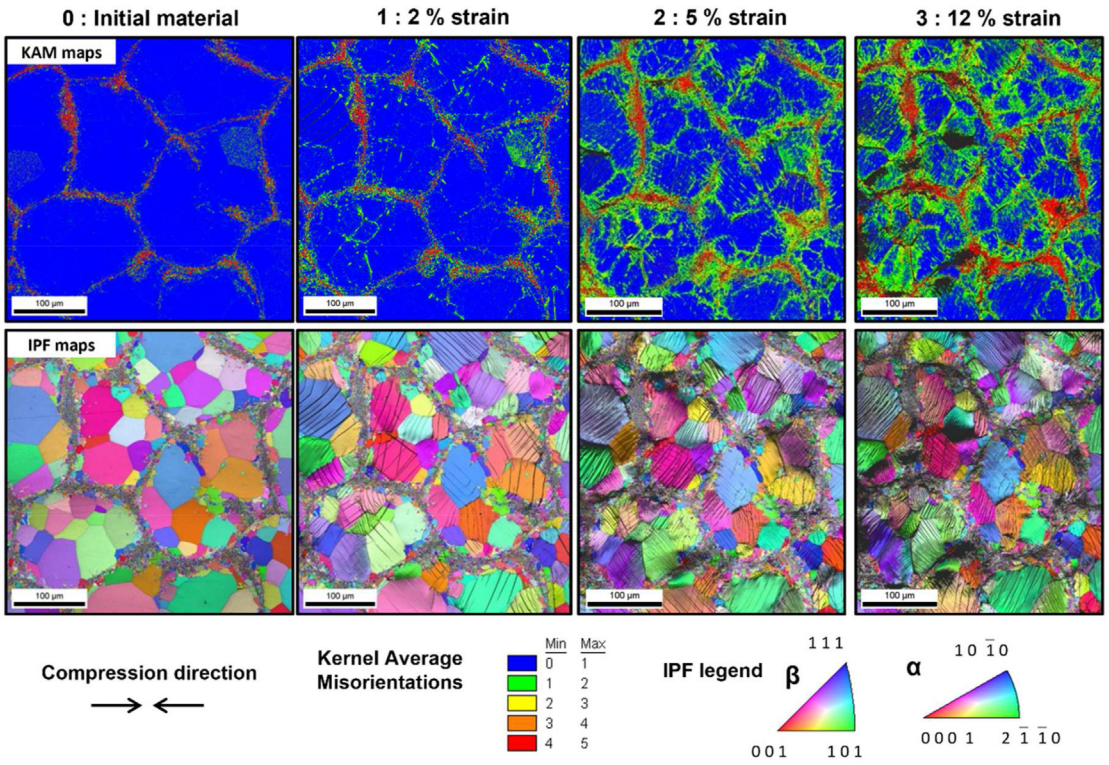

Fig. 6 – EBSD analysis of the evolution of the microstructure during compression tests for sample SPS – 60 min. KAM (top) and IPF (bottom) maps for the initial sample SPS – 60 min and after compression up to 2, 5, and 12% strains.

the shell as discussed above). Regions with large strain gradients formed near interfaces during plastic deformation are often called Interface Affected Zone (IAZ) [42]. The width of the IAZ for sample SPS – 60 min increased with plastic strain, as revealed from the comparison of the KAM maps taken at 5% and 12% strains. It is also revealed that the magnitude of strain gradients increased with plastic strain [23]. Namely, piling up of dislocations may occur at the interfaces between hard and soft domains – which are the shell and the core parts, respectively – to accommodate the deformation heterogeneities induced by hardness differences in the material (see section 3.1). This piling-up of dislocations at core-shell interfaces should induce HDI stresses, resulting in a high work hardening in the first percentages of plastic deformation. Still, further TEM observations of the core-shell interfaces are needed to observe the actual arrangement of dislocations at the interfaces.

The EBSD images in Fig. 7 show the microstructure of sample SPS – 60 min at high strains of 15% and 20%. According to Fig. 7, the misorientations are not located in the shell vicinity at high strain percentages, unlike in the early stages of plasticity. On the contrary, they increased inside the core, which is most probably associated with the rise of the dislocation density in the core part of the microstructure. It should thus be noted that from 5% strain, grain boundaries in the core also act as localization sites of strain in the material; and as a result, IAZ are also formed near grain boundaries of the core. From 5% strain, most of the misorientations inside the core are located at grain boundaries, as confirmed, for instance, in the KAM image obtained for sample SPS – 60 min deformed up to the strain of 12%.

In contrast, the interiors of the coarse grains in the core are much less distorted. An interpretation of this observation is that grain boundaries can play the same role at high plastic strains as the shell at a lower plastic strain. Pile-ups of dislocations formed at the grain boundaries in the core can also result in HDI stresses.

A surface density of LAGBs with misorientations lower than 15° (the length of LAGBs in a unit surface area) was calculated at each stage of the deformation process. The evolution of this parameter is plotted in Fig. 8 as a function of the compression strain. The graph combines the results obtained via EBSD at low and moderate strains (black symbols) and high strains (red symbols). The LAGB density increased monotonously with increasing the strain during compression of the harmonic-structured sample SPS – 60 min. In addition, no martensitic phase transformation nor twinning – neither $\{332\}\langle 113\rangle_{\beta}$ nor $\{112\}\langle 111\rangle_{\beta}$ – was observed in the deformed microstructures of the present harmonic-structured Ti–24Nb–4Zr–8Sn alloy. Such deformation mechanisms have been suggested in former studies [25,43,44]. The presence of $\{332\}\langle 113\rangle_{\beta}$ twins in the deformed microstructures of metastable β-titanium alloys is usually linked with a martensitic phase transformation, as they are the traces of the previously formed $\{130\}\langle 310\rangle_{\alpha''}$ twins in the martensite. As a result, the absence of twins in the microstructure, combined

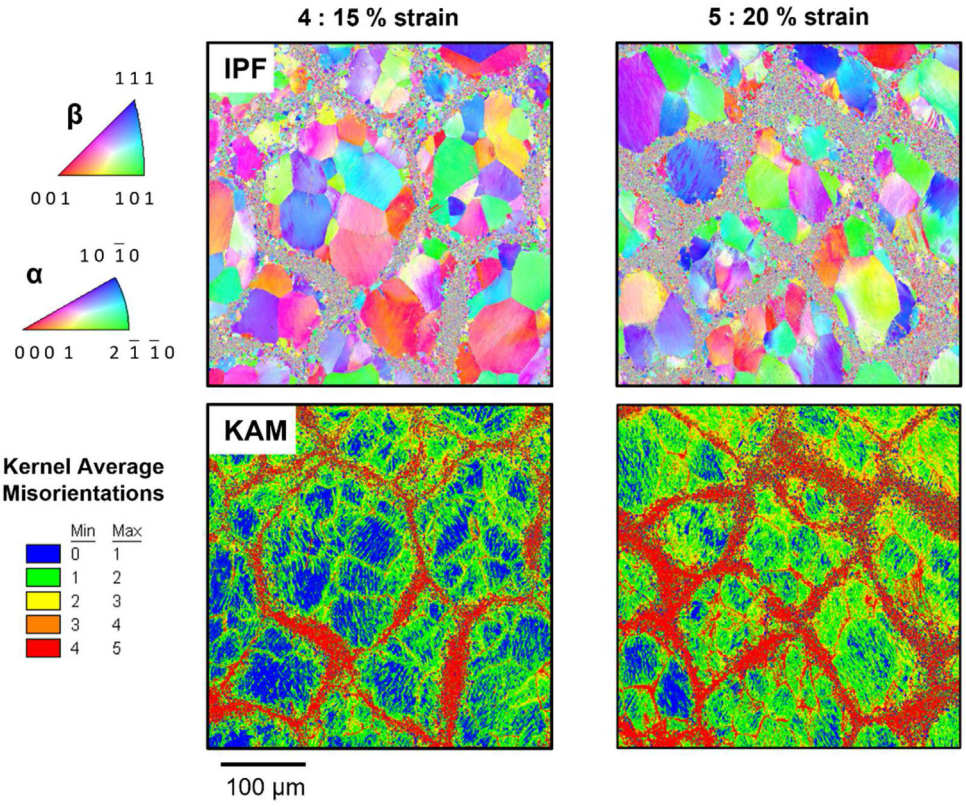

Fig. 7 – EBSD investigation (IPF- top - and KAM maps - bottom) of sample SPS – 60 min at 15% compression strain and at the end of compression test (20% strain).

with the conventional shape of the compression curves (the elastic domain is linear, and the plastic domain has a conventional shape), led to the conclusion that martensitic transformation is suppressed in the studied harmonic structures. Therefore, the critical stress to induce martensitic transformation may drastically increase when Ti–24Nb–4Zr–8Sn is harmonically structured.

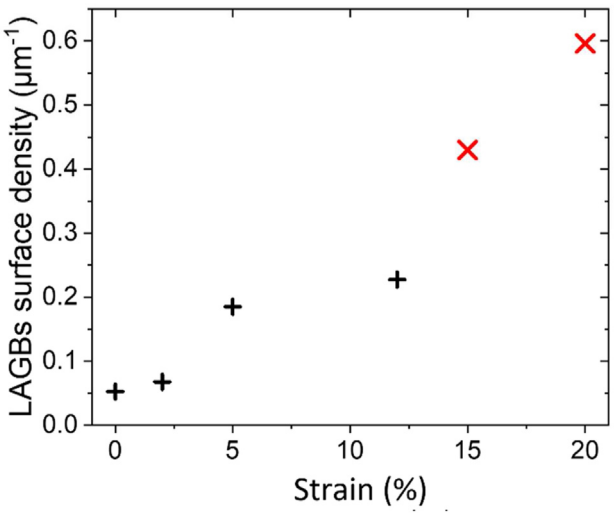

Fig. 8 – Evolution of LAGB density (LAGBs length in a unit area) as a function of compressive strain for sample SPS – 60 min. The black and red crosses represent data obtained by EBSD analysis performed for low/moderate and high strains, respectively (see Fig. 6 and 7).

The following arguments could explain the absence of martensite and twins in the deformed harmonic microstructure. First, the harmonic microstructure has already been proven to inhibit twinning during deformation of other β-titanium alloys [45]. The same may be valid for martensitic transformation, as {332}<113>$_\beta$ twinning mode and TRIP may be closely linked in metastable β-titanium alloys. This effect could be easily understood since grain size also plays an essential role in twinning and martensitic transformation mechanisms [46]. TRIP and TWIP effects are hindered in fine-grained metastable β-titanium alloys. Nevertheless, no martensite is detected in the coarse grains of the core of the presently studied harmonic microstructure. In that case, martensitic transformation inhibition could be linked with the oxygen enrichment of the alloy during the sample processing. Indeed, oxygen strongly influences β phase stability and the precipitation sequence in the β phase during thermal treatments or plastic deformation [47]. It is also a suitable controller of the martensitic transformation in Ti–24Nb–4Zr–8Sn, drastically lowering the martensite start temperature (Ms) [48].

Finally, plasticity mechanisms also depend on the mechanical loading mode. It has been shown in former unpublished studies that different plasticity mechanisms occurred depending on the type of loading mode - tensile or compressive tests, shear, rolling, etc. For example, when conventional Ti–24Nb–4Zr–8Sn alloy is mechanically tested in tension or

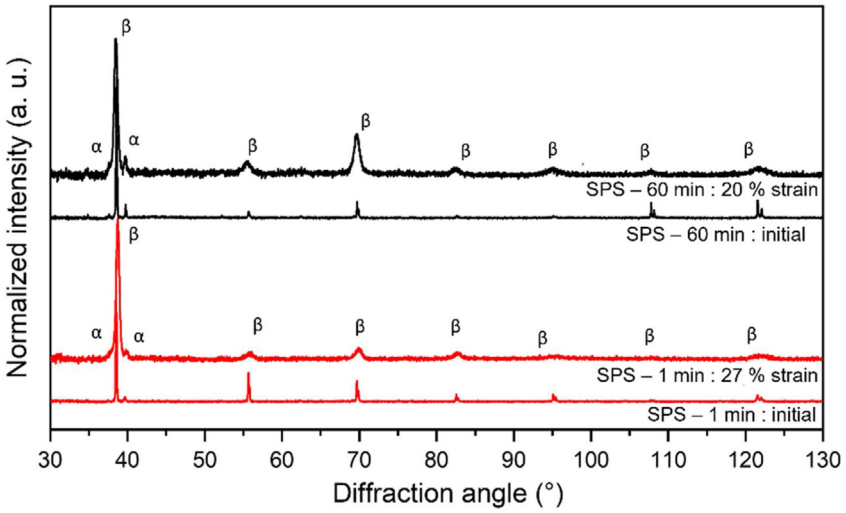

Fig. 9 – XRD diffractograms for SPS – 1 min (red) and SPS – 60 min (black) samples before (bottom) and after (top) compression tests (at a respective compression strain of 27% for SPS – 1 min and 20% for SPS – 60 min samples).

compression, only dislocations are detected in the deformed microstructure using the EBSD method. On the contrary, twins are formed in the material when the same conventional structure of Ti–24Nb–4Zr–8Sn alloy is cold rolled. They have been observed via EBSD analysis at a thickness reduction of 20% and 45%. Moreover, BM has also been proven to induce the formation of {332}<113>$_\beta$ twins in Ti–24Nb–4Zr–8Sn powder particles.

3.3. *XRD analysis of the deformed harmonic microstructures at different strains*

In addition to the EBSD analysis, both SPS – 1 min and SPS – 60 min samples were investigated before and after compression tests by XRD, and the corresponding patterns are presented in Fig. 9. Initially, both samples are composed of β and α phases, as it was expected based on EBSD measurements. A slightly higher intensity of the main XRD peak of the α phase was observed for sample SPS - 60 min compared to specimen SPS - 1 min for both the initial and the compressed states. This slight difference is associated with the higher volume fraction of α phase in SPS – 60 min sample in comparison with the specimen SPS – 1 min. This observation is in accordance with the EBSD results obtained on the α phase fraction (see Table 1). The slightly broader α peaks for SPS - 1 min sample also suggests a smaller size of α precipitates compared to the specimen SPS – 60 min.

Fig. 9 shows an evident broadening of the peaks of the β phase during compression. This broadening could be associated with a significant decrease in the crystallite size in the material and/or with a multiplication of dislocations. In addition, the possible arrangement of dislocations into cells or LAGBs during plastic deformation may also change the XRD peak breadth. Therefore, a detailed evaluation of the XRD peak profiles was performed using the CMWP fitting method [49]. This method requires the Burgers vector of dislocations as an input parameter. As the β phase has a bcc structure, we consider that the following slip system is activated during plastic deformation: 1/2<111>{110}$_\beta$. Thus, the magnitude of the Burgers vector ***b*** can be obtained from the lattice constant a as $b = a\sqrt{3}/2$. The lattice parameter of the β phase is determined by Rietveld refinement on XRD measurements of β-Ti-24Nb–4Zr–8Sn [33] and confirmed by other studies [48]. A value of 3.30 Å was found for the lattice constant, and consequently, a value of 2.86 Å was calculated for the Burgers vector of dislocations. In the CMWP fitting procedure, a parameter denoted as q describes the material's edge/screw character of dislocations. The values of q for complete edge and screw dislocations were calculated based on the anisotropic elastic constants of the β phase. They have been determined for β phase with Ti–24Nb–4Zr–8Sn composition by resonant ultrasound spectroscopy by Zhang et al. [50]. Models for determining these values, which have been

Table 2 – Results of XLPA for the main bcc β phase in samples SPS – 1 min and SPS – 60 min after compression deformation up to the strain of 15% and at the end of the compression tests, which corresponds to the strains of 27% and 20% for samples SPS -1 min and SPS – 60 min, respectively. $\langle x \rangle_{area}$, ρ and M are the area-weighted mean crystallite size, the dislocation density, and the dislocation arrangement parameter, respectively.

Sample	Compression strain (%)	$\langle x \rangle_{area}$ (nm)	Dislocation density, ρ (10^{14} m^{-2})	Dislocation arrangement parameter, M
SPS - 1 min	15	38 ± 5	77 ± 8	6.4 ± 0.6
	27	23 ± 3	87 ± 9	5.2 ± 0.5
SPS - 60 min	15	32 ± 4	55 ± 6	6.3 ± 0.6
	20	35 ± 5	48 ± 5	5.2 ± 0.5

performed by Obbard et al., are also in agreement with the experimental results [48]. Based on these data, the q values for perfect edge and screw dislocations are 1.75 and 2.73, respectively. Values in between are associated with a mixed character of dislocations.

Accurate fittings of the experimental diffractograms allow for determining several microstructural parameters in the β phase, which are listed in Table 2. For instance, Fig. 10 shows the CMWP fitting for sample SPS - 60 min, which was compressed up to the strain of 20%. The fitting is excellent, as revealed by the practically zero difference between the measured and calculated diffraction patterns. Similar fittings were performed for the other samples at different compression strain percentages. It should be noted that for the initial samples before compression, the dislocation density was lower while the crystallite size was larger than the detection limit of XLPA (about 10^{13} m^{-2} and 1 μm, respectively). Therefore, this method cannot characterize the microstructure of the β phase in the SPS-processed specimens.

As the final strains at the end of the compression tests are different in samples SPS − 1 min and SPS − 60 min, the compression tests were interrupted at the same strain of 15%, and XLPA studied the corresponding samples. The results can be compared in Table 2. For both samples, a low crystallite size of about 30–40 nm and a high dislocation density of $55–77 \times 10^{14}$ m^{-2} were obtained at the compression strain of 15%. The crystallite size determined by XLPA is much lower than the grain size obtained by EBSD. This difference is because misorientations at the grain boundaries are at least 15° per definition, while the low-angle misorientations also influence the results of XLPA. Therefore, the crystallite size or coherently scattering domain size obtained by XLPA gives the dimension of dislocation cells and subgrains bounded by LAGBs, not the grain size.

The dislocation density values determined by XLPA for the compressed samples are very high compared to the initial

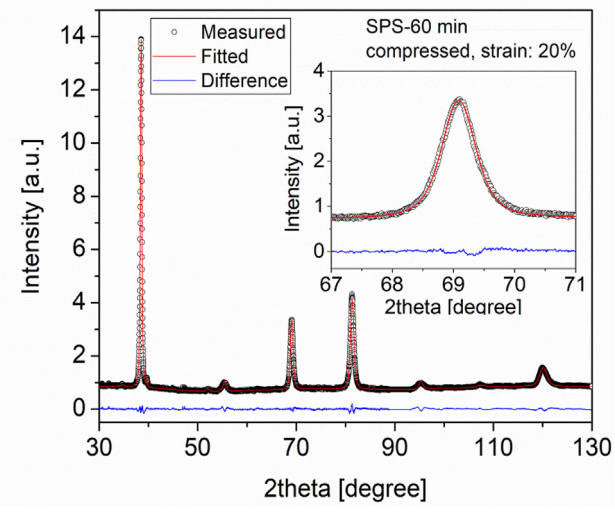

Fig. 10 − CMWP fitting for sample SPS-60 min compressed up to the strain of 20%. The open circles and the solid line represent the measured and calculated patterns in the best fitting case. The difference between the measured and calculated data is shown at the bottom of the figure. A magnified part of the pattern is shown in the inset.

state (at least 2–3 orders of magnitude higher), which suggests a strong ability of harmonic-structured Ti–24Nb–4Zr–8Sn alloy to work hardening. Indeed, the dislocation density is much lower for other bcc alloys at similar compressive strains. For instance, for a bcc high-entropy alloy with the composition of HfNbTaTiZr after compression at a strain of 20%, the dislocation density was only about 15×10^{14} m^{-2} [51]. Sample SPS − 1 min had a higher value of the dislocation density than sample SPS − 60 min; this could be explained by the higher hardness values of the shell of SPS − 1 min than the shell of SPS − 60 min, inducing a stronger work hardening ability of the material. However, dislocation densities are high for both samples. The *q* values given by the CMWP fitting method is about 2.1 for both compressed samples, which is slightly lower than the average of the theoretical values for pure edge and screw dislocations (2.24). Therefore, it can be concluded the dislocations have a mixed character. CMWP fitting also gives the dislocation arrangement parameter, *M*. This parameter is associated with the outer cut-off radius of the elastic strain field of dislocations in the material. The lower the value of *M*, the more shielded the strain field of dislocations. This can occur when dislocations are arranged into dipoles or LAGBs. Table 2 suggests no significant difference exists between the dislocation arrangements in samples SPS − 1 min and SPS − 60 min.

The evolution of the microstructure during compression was studied by comparing the XLPA results obtained at the strain of 15% and the end of the compression tests corresponding to the strains of 27% and 20% for samples SPS - 1 min and SPS − 60 min, respectively. The crystallite size of specimen SPS − 1 min decreased when the strain increased from 15 to 27%, while the size of crystallites remained unchanged for sample SPS − 60 min between the strains 15 and 20%. The difference is probably caused by the much smaller increase in strain for the latter specimen. For both samples, the dislocation density did not change significantly with increasing strain. On the other hand, the dislocation arrangement parameter decreased slightly from 6.4 ± 0.6 to 5.2 ± 0.5 for sample SPS − 1 min and from 6.3 ± 0.6 nm to 5.2 ± 0.5 nm for specimen SPS - 60 min when the strain increases. This change in the value of *M* indicates that the strain fields of dislocations tend to screen one another when plastic strain increases, which is most probably related to the arrangement of dislocations into cell boundaries and LAGBs. Parameter *q* describing dislocations' edge/screw character is still intermediate, suggesting a mixed character of dislocations. This is in accordance with the previous experimental observations presented above. Indeed, the screw component of the dislocations can cross-slip, which is visible in the slip bands in Fig. 5. However, many dislocation pile-ups are also detected at core-shell interfaces (see Fig. 6), and this spatial arrangement of dislocations usually forms with rather edge dislocations, as this type of dislocations cannot cross-slip to another plane in the vicinity of the obstacle [52].

3.4. *Damage initiation in the harmonic material*

The initiation of damage during compression was finally studied, which revealed the dual effect of the shell on the mechanical behavior of the harmonic microstructure. Namely,

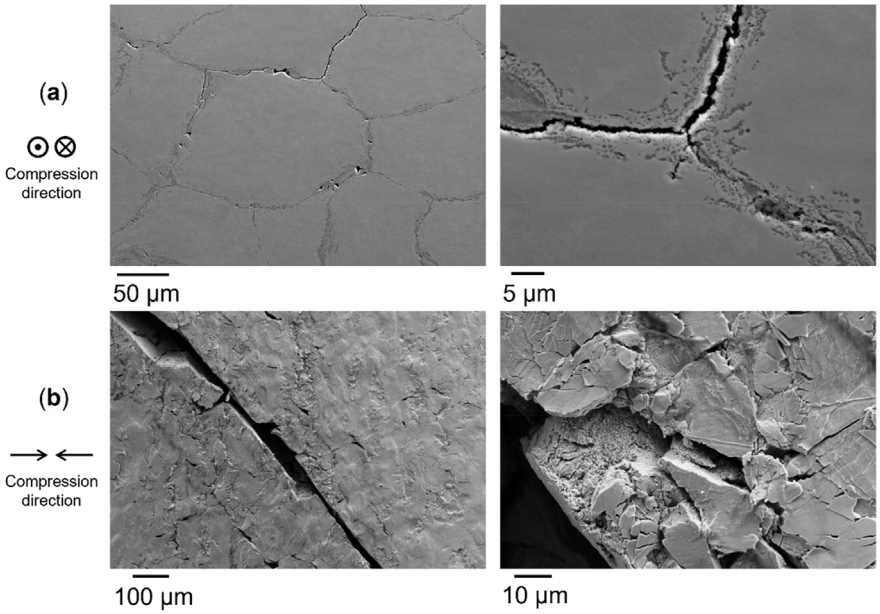

Fig. 11 – SEM images of the surface of SPS - 1 min sample after compression up to failure, taken perpendicular (a) and parallel (b) to the compression direction, showing the formation and propagation of cracks in the shell.

the shell plays a key role as an HDI stress concentration site in the work-hardening behavior of harmonic-structured Ti–24Nb–4Zr–8Sn alloy. Therefore, the shell contributes to creating and storing a high density of dislocations. However, the shell is also where damage initiates in the material.

Fig. 11 illustrates the presence of cracks in the shell of sample SPS - 1 min, fractured by compression. Fig. 11(a) and (b) show SEM images taken perpendicular and parallel to the compression direction, respectively. The nucleation and propagation of cracks lead to a failure of the material, and the fine-grained and oxygen-rich shell is the preferential path for the propagation of cracks. Such a typical crack is shown in Fig. 11(b): it has formed in an orientation of 45° with regards to the compression direction, and its path follows the shell's profile. The very straight shape of the crack is characteristic of a brittle fracture behavior.

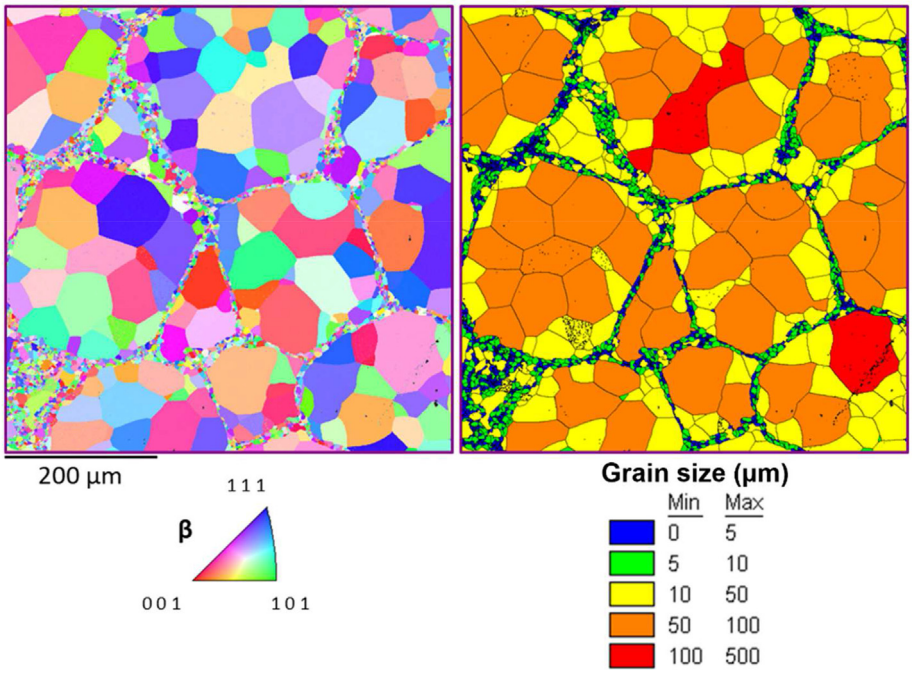

Fig. 12 – EBSD IPF and grain size maps for Ti–24Nb–4Zr–8Sn harmonic sample without α precipitates. BM has been performed under vacuum. SPS was carried out for 60 min.

4. Discussion

In this section, we analyze the contributions of the different microstructural elements to the 0.2% proof stress and the work hardening performance for sample SPS – 60 min. To clarify the effect of α precipitates on the strength, we compared the compression behavior of SPS – 60 min sample with a similar harmonic material, whose BM was performed for the same duration but under vacuum conditions, and therefore the material contains only negligible oxygen and consequently very few α precipitates. These precipitates appeared only at triple points of core-shell structures, and the volume fraction of precipitates was below the detection limit of XRD. The microstructure of the sample without α precipitates is shown in Fig. 12, and the compression behavior of the samples with and without α phase is compared in Fig. 13. Fig. 13 shows the influence of α phase precipitates and oxygen content on the compression stress. As oxygen is a strong α-stabilizer element in titanium alloys, oxygen would favor the precipitation of α phase and segregate in these precipitates. Therefore, these two microstructural features (oxygen content and α phase precipitates) cannot be easily considered independently. Fig. 13 shows that the flow stress values obtained for the harmonic sample with α phase precipitates are about 220 MPa higher than the values for the specimen processed under vacuum. Therefore, this value can estimate the contribution of both α phase and oxygen solid solution on compression yield strength ($\sigma_{(\alpha+\text{oxygen})}$).

The contribution of the grain size to the proof stress was calculated for both samples SPS – 1 min and SPS – 60 min using the Hall-Petch formula determined from tensile results obtained on conventional Ti–24Nb–4Zr–8Sn alloy samples processed by powder metallurgy routes and having different grain sizes. The samples used for determining Hall-Petch coefficients were Ti–24Nb–4Zr–8Sn conventional structures (non-harmonic) with monomodal grain size distribution. The Hall-Petch relationship between the average grain size (d) and its contribution to the proof stress (σ_{HP}) is given as:

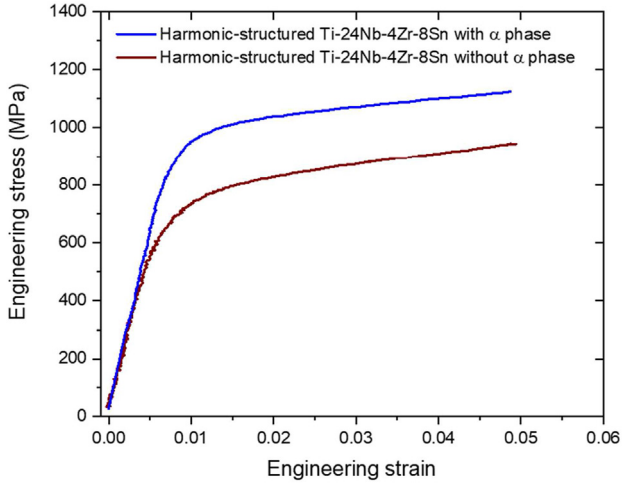

Fig. 13 – Comparison of the compression behavior of harmonic Ti–24Nb–4Zr–8Sn samples with and without α precipitates.

$$\sigma_{HP} = \sigma_0 + k/\sqrt{d}\,, \tag{2}$$

where the values of σ_0 and k are determined as 518 MPa and 746 MPa $\mu m^{0.5}$, respectively, which are in good agreement with those presented in the literature for Ti–24Nb–4Zr–8Sn alloy [53]. Using these Hall-Petch parameters and the average of the grain sizes of the core and the shell parts (see Table 1) weighted with their volumes, the grain size strengthening σ_{HP} was obtained as 716 MPa for SPS – 60 min. It should be noted that the use of a rule of mixture for the calculation of the grain size strengthening does not consider the mechanical contrast effect created by the core-shell structure and avoid the effect of the synergy which occurs between these volumes during plastic flow. However, the calculation presented above is performed only for the proof stress at the beginning of deformation, and the synergy effect of the core-shell structure that can be pronounced in the hardening behavior will be discussed later in this study.

A simple summation of the calculated σ_{HP} and $\sigma_{(\alpha+\text{oxygen})}$ contributions gives a value of 936 MPa for the proof stress ($R_{e,0.2}$), which is very close to $R_{e,0.2}$ determined experimentally from the stress-strain curve (945 MPa). The dislocation strengthening contribution should be very low due to the negligible dislocation density at the beginning of compression, as revealed by XLPA. It is worth noting that the addition rule of the different strength contributions is not known, and the linear summation law was used here only because this is the simplest one.

The maximum compression stress accounts for work hardening, and we propose here a discussion about the sources of work hardening of harmonic Ti–24Nb–4Zr–8Sn samples. A comparison of the strain hardening rates for the samples with and without α precipitates in Fig. 13 revealed that the α phase precipitates and the associated oxygen enrichment in the shell do not increase the work hardening of harmonic-structured materials considerably. EBSD showed that the grain size did not change during compression, while XLPA revealed a considerable increase in the dislocation density. The hardening caused by dislocations ($\sigma_{dislocation}$) can be obtained using the Taylor formula:

$$\sigma_{dislocation} = M\alpha\mu b\sqrt{\rho}, \tag{3}$$

where M is the Taylor factor of the material, which is considered equal to 3 because of the random texture of the sample, $\alpha = 0.3$, μ is the shear modulus of the material, which is determined during shear tests of similar harmonic Ti–24Nb–4Zr–8Sn samples and taken equal to 20.9 GPa [33]. The contribution of dislocations to the flow stress at the strain of 15% was calculated as 399 ± 117 MPa for sample SPS – 60 min. This result suggests that about one-third of the total measured flow stress at the end of compression (about 1300 MPa, see Fig. 3) can be related to the strengthening effect of dislocations.

The pile-ups of dislocations formed at glide obstacles, such as the shell in harmonic-structured materials, yield back stress in the core. The back stress (σ_b) resulting from these pile-ups is proportional to the number of dislocations in the pile-ups (N) and inversely proportional to the length of the pile-up (Λ) [21] according to the following equation:

$$\sigma_b = \frac{N\mu b}{2\pi\Lambda}. \quad (4)$$

The back stresses may be different in samples SPS – 1 min and SPS - 60 min due to the various microstructures in the shell of the two specimens. The microstructural features may influence the strain gradient which is created at core-shell interfaces, and consequently the length of the pile-ups and the number of dislocations in the pile-ups.

Several methods have been proposed in the literature to quantify the back stress from the loading-unloading stress-strain curves [18,54]. One was used to evaluate the back stress in the SPS – 60 min sample using the compression curve in Fig. 3. In this procedure, a straight line is fitted to the linear segment of the unloading part of the stress-strain curve as shown in Fig. 14. The ends of the linear part of the unloading curve were determined using the following criterion: the deviation between the slopes of the tangents fitted to the different points of the linear segment cannot be higher than ±10%. Many discussions exist in the literature on whether an offset or slope reduction criterion should be considered to determine the ends of the linear part of the unloading curve. Slope reduction criterion seems to be more accurate, giving results with a lower scattering and having a physical meaning. For instance, a 10% deviation of the slope physically means that 10% of the volume of the material is no longer in the elastic domain and deforms plastically [55]. Fig. 14 shows that the back stress was calculated as the average stress values corresponding to the ends of the linear unloading segment.

Using this method, we can calculate the back stress for SPS – 60 min sample. It equals 641 MPa at the strain of 2% and 646 MPa at the strain of 5%. It contributes to the hardening of the initially soft part of the material (the core). In addition, dislocation pile-ups formed at the core-shell interfaces cause forward stress in the shell which yields softening of the initially hard part of the material (the shell) and finally led to a progressive homogenization of the deformation of the initially heterogeneous material.

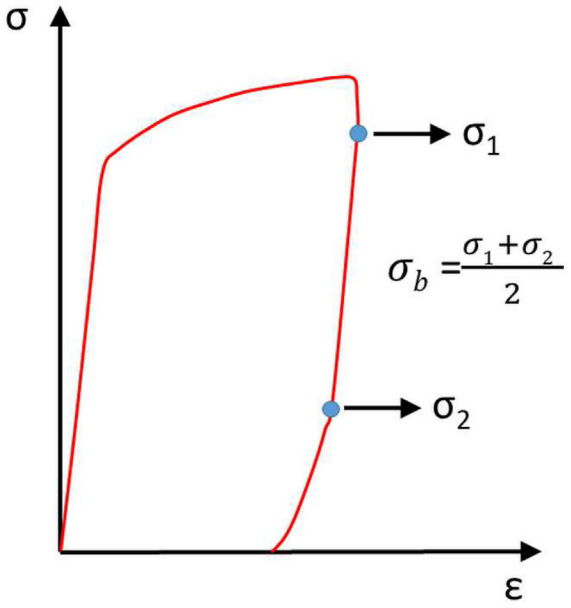

Fig. 14 – A schematic showing the back stress (σ_b) determination from the unloading stress-strain curve for sample SPS – 60 min.

5. Conclusions

SEM, EBSD and XRD experiments were conducted for studying the microstructure evolution in a harmonic-structured Ti–24Nb–4Zr–8Sn alloy during compression. The main conclusions are summarized below.

- The harmonic-structured Ti–24Nb–4Zr–8Sn alloys SPS-processed for 1 and 60 min reached a high compressive proof stress of about 1 GPa. The strain hardening rate was shown to depend on the grain size differences between the core and the shell.
- A high dislocation density is detected in the material after compression deformation (several tens of 10^{14} m^{-2}). Dislocations also tend to form cells and LAGBs during compression.
- Dislocations first localized at the core-shell interfaces for low plastic strains (about 2%), where they are a substantial source of HDI stress in the material. The calculated back stress was about 640 MPa after compression at 2–5% strains. At higher plastic strains, dislocation density also increased in the core. In this process, the accumulation of dislocations started at the grain boundaries of the core, which might have also caused internal stresses.
- No trace of transformation-induced plasticity or twinning-induced plasticity is detected during the compression of harmonic-structured Ti–24Nb–4Zr–8Sn alloy.
- Grain size heterogeneities in the microstructure are supposed to enhance the work hardening of the material. However, it was found that the α phase and the oxygen contents contribute to the proof stress but not the strain hardening during the compression test of harmonic-structured Ti–24Nb–4Zr–8Sn alloy. These two features influence the hardness of the shell and, therefore, the shell interface's efficiency in generating HDI stress inside the material.
- The experimentally determined proof stress was successfully obtained as the sum of the calculated contributions related to the grain size and the α phase/oxygen contents.
- It was shown that the shell is the preferential site for crack initiation and propagation in the studied harmonic structure, which then yields failure of the material.

Data availability

Data will be made available on request.

Declaration of competing interest

The authors declare that they have no known competing financial interests or personal relationships that could have appeared to influence the work reported in this paper.

Acknowledgments

The French National Research Agency supported this work in the framework of the ANR 14-CE07-0003 "HighS-Ti" program. B. Fer thanks École Doctorale Galilée, University Sorbonne Paris Nord for their financial support. B. Fer carried out a part of the present work at Eötvös Loránd University, Budapest, Hungary.

Appendix A. Supplementary data

Supplementary data to this article can be found online at https://doi.org/10.1016/j.jmrt.2023.07.250.

REFERENCES

[1] Ritchie RO. The conflicts between strength and toughness. Nat Mater 2012;10(11). https://doi.org/10.1038/nmat3115.
[2] Wu SW, Wang G, Wang Q, Jia YD, Yi J, Zhai QJ, et al. Enhancement of strength-ductility trade-off in a high-entropy alloy through a heterogeneous structure. Acta Mater 2019;165:444–58. https://doi.org/10.1016/j.actamat.2018.12.012.
[3] Yin Z, Yang X, Ma X, Moering J, Yang J, Gong Y, et al. Strength and ductility of gradient structured copper obtained by surface mechanical attrition treatment. Mater Des 2016;105:89–95. https://doi.org/10.1016/j.matdes.2016.05.015.
[4] Shin S, Zhu C, Zhang C, Vecchio KS. Extraordinary strength-ductility synergy in a heterogeneous-structured β -Ti alloy through microstructural optimization. Mater Res Lett 2019;7:11. https://doi.org/10.1080/21663831.2019.1652856.
[5] Jiang F, Zhao C, Liang D, Zhu W, Zhang Y, Pan S, et al. In-situ formed heterogeneous grain structure in spark-plasma-sintered CoCrFeMnNi high-entropy alloy overcomes the strength-ductility trade-off. Mater Sci Eng, A 2020;771:138625. https://doi.org/10.1016/j.msea.2019.138625.
[6] Wang Z, Lin X, Kang N, Hu Y, Chen J, Huang W. Strength-ductility synergy of selective laser melted Al-Mg-Sc-Zr alloy with a heterogeneous grain structure. Addit Manuf 2020;34:101260. https://doi.org/10.1016/j.addma.2020.101260.
[7] Vajpai SK, Ota M, Zhang Z, Ameyama K. Three-dimensionally gradient harmonic structure design: an integrated approach for high performance structural materials. Mater. Res. Lett. 2016;4:4. https://doi.org/10.1080/21663831.2016.1218965.
[8] Dirras G, Gubicza J, Ramtani S, Bui QH, Szilágyi T. Microstructure and mechanical characteristics of bulk polycrystalline Ni consolidated from blends of powders with different particle size. Mater Sci Eng, A 2012;527:4. https://doi.org/10.1016/j.msea.2009.09.050.
[9] Zhang Z, Vajpai SK, Orlov D, Ameyama K. Improvement of mechanical properties in SUS304L steel through the control of bimodal microstructure characteristics. Mater Sci Eng, A 2014;598:106–13. https://doi.org/10.1016/j.msea.2014.01.023.
[10] Rai PK, Shekhar S, Yagi K, Ameyama K, Mondal K. Fretting wear mechanism for harmonic, non-harmonic and conventional 316L stainless steels. Wear 2019;424–425:23–32. https://doi.org/10.1016/j.wear.2019.02.005.
[11] Vajpai SK, Sawangrat C, Yamaguchi O, Ciuca OP, Ameyama K. Effect of bimodal harmonic structure design on the deformation behaviour and mechanical properties of Co-Cr-Mo alloy. Mater Sci Eng C 2016;58:1008–15. https://doi.org/10.1016/j.msec.2015.09.055.
[12] Dirras G, Ota M, Tingaud D, Ameyama K, Sekiguchi T. Microstructure evolution during direct impact loading of commercial purity α -titanium with harmonic structure design: direct impact loading of pure harmonic α -Ti. Mater Technol 2015;103:3. https://doi.org/10.1051/mattech/2015031.
[13] Kikuchi S, Hayami Y, Ishiguri T, Guennec B, Ueno A, Ota M, et al. Effect of bimodal grain size distribution on fatigue properties of Ti-6Al-4V alloy with harmonic structure under four-point bending, Mater Sci Eng A;687,269-275, https://doi.org/10.1016/j.msea.2017.01.076.
[14] Ameyama K, Cazes F, Couque H, Dirras G, Kikuchi S, Li J, et al. Harmonic structure, a promising microstructure design. Mater. Res. Lett. 2022;10(7):440–71. https://doi.org/10.1080/21663831.2022.2057203.
[15] Ashby MF. The deformation of plastically non-homogeneous materials. Philos. Mag. J. Theor. Exp. Appl. Phys. 1970;21(170):399–424. https://doi.org/10.1080/14786437008238426.
[16] Kassner ME, Geantil P, Levine LE. Long range internal stresses in single-phase crystalline materials. Int J Plast 2013;45:44–60. https://doi.org/10.1016/j.ijplas.2012.10.003.
[17] Park HK, Ameyama K, Yoo J, Hwang H, Kim HS. Additional hardening in harmonic structured materials by strain partitioning and back stress. Mater. Res. Lett. 2018;6:5. https://doi.org/10.1080/21663831.2018.1439115.
[18] Yang M, Pan Y, Yuan F, Zhu Y, Wu X. Back stress strengthening and strain hardening in gradient structure. Mater. Res. Lett. 2016;4:3. https://doi.org/10.1080/21663831.2016.1153004.
[19] Zhu Y, Wu X. Perspective on hetero-deformation induced (HDI) hardening and back stress. Mater. Res. Lett. 2019;7(10):393–8. https://doi.org/10.1080/21663831.2019.1616331.
[20] Cao Y, Zhang W, Liu B, Song M, Liu Y. Extraordinary tensile properties of titanium alloy with heterogeneous phase-distribution based on hetero-deformation induced hardening. Mater. Res. Lett. 2020;8(7):254–60. https://doi.org/10.1080/21663831.2020.1745919.
[21] Mompiou F, Tingaud D, Chang Y, Gault B, Dirras G. Conventional vs harmonic-structured β-Ti-25Nb-25Zr alloys: a comparative study of deformation mechanisms. Acta Mater 2018;161:420–30. https://doi.org/10.1016/j.actamat.2018.09.032.
[22] Zhou H, Huang C, Sha X, Xiao L, Ma X, Höppel HW, et al. In-situ observation of dislocation dynamics near heterostructured interfaces. Mater. Res. Lett. 2019;7(9):376–82. https://doi.org/10.1080/21663831.2019.1616330.
[23] Wang YF, Wang MS, Fang XT, Guo FJ, Liu HQ, Scattergood RO, et al. Extra strengthening in a coarse/ultrafine grained laminate: role of gradient interfaces. Int J Plast 2019;123:196–207. https://doi.org/10.1016/j.ijplas.2019.07.019.
[24] Hao YL, Li SJ, Sun SY, Zheng CY, Yang R. Elastic deformation behaviour of Ti–24Nb–4Zr–7.9Sn for biomedical applications. Acta Biomater 2007;3:2. https://doi.org/10.1016/j.actbio.2006.11.002.
[25] Zhang SQ, Li SJ, Jia MT, Prima F, Chen LJ, Hao YL, et al. Low-cycle fatigue properties of a titanium alloy exhibiting nonlinear elastic deformation behavior. Acta Mater 2011;59(11):4690–9. https://doi.org/10.1016/j.actamat.2011.04.015.
[26] Yang Y, Castany P, Cornen M, Prima F, Li SJ, Hao YL, et al. Characterization of the martensitic transformation in the superelastic Ti–24Nb–4Zr–8Sn alloy by in situ synchrotron X-ray diffraction and dynamic mechanical analysis. Acta Mater 2015;88:25–33. https://doi.org/10.1016/j.actamat.2015.01.039.

[27] Hao YL, Li SJ, Prima F, Yang R. Controlling reversible martensitic transformation in titanium alloys with high strength and low elastic modulus. Scripta Mater 2012;67(5):487–90. https://doi.org/10.1016/j.scriptamat.2012.06.011.
[28] Wang HL, Hao YL, He SY, Li T, Cairney JM, Wang YD, et al. Elastically confined martensitic transformation at the nano-scale in a multifunctional titanium alloy. Acta Mater 2017;135:330–9. https://doi.org/10.1016/j.actamat.2017.06.040.
[29] Liang Q, Kloenne Z, Zheng Y, Wang D, Antonov S, Gao Y, et al. The role of nano-scaled structural non-uniformities on deformation twinning and stress-induced transformation in a cold rolled multifunctional β-titanium alloy. Scripta Mater 2020;177:181–5. https://doi.org/10.1016/j.scriptamat.2019.10.029.
[30] Yao T, Du K, Wang H, Huang Z, Li C, Li L, et al. In situ scanning and transmission electron microscopy investigation on plastic deformation in a metastable β titanium alloy. Acta Mater 2017;133:21–9. https://doi.org/10.1016/j.actamat.2017.05.018.
[31] Yang Y, Castany P, Bertrand E, Cornen M, Lin JX, Gloriant T. Stress release-induced interfacial twin boundary ω phase formation in a β type Ti-based single crystal displaying stress-induced α" martensitic transformation. Acta Mater 2018;149:97–107. https://doi.org/10.1016/j.actamat.2018.02.036.
[32] Ribárik G, Gubicza J, Ungár T. Correlation between strength and microstructure of ball-milled Al–Mg alloys determined by X-ray diffraction. Mater Sci Eng, A 2004;387–389:343–7. https://doi.org/10.1016/j.msea.2004.01.089.
[33] Fer B, Tingaud D, Hocini A, Hao Y, Leroy E, Prima F, et al. Powder metallurgy processing and mechanical properties of controlled Ti-24Nb-4Zr-8Sn heterogeneous microstructures. Metals 2020;10:12. https://doi.org/10.3390/met10121626.
[34] Li W, Zeng F, Li L, Wang Z, Liu H, Peng Y, et al. Spark plasma sintering of Ti–1Al–8V–5Fe alloy: densification mechanism and grain growth. Appl Phys A 2020;126(9):709. https://doi.org/10.1007/s00339-020-03911-w.
[35] Bartáková S, Málek J, Prachár P. The effect of oxygen addition on microstructure and mechanical properties of various beta-titanium alloys. J Occup Med 2020;72(4):1656–63. https://doi.org/10.1007/s11837-019-03879-w.
[36] Prithiv TS, Kloenne Z, Li D, Shi R, Zheng Y, Fraser HL, et al. Grain boundary segregation and its implications regarding the formation of the grain boundary α phase in the metastable β-Titanium Ti–5Al–5Mo–5V–3Cr alloy. Scripta Mater 2022;207:114320. https://doi.org/10.1016/j.scriptamat.2021.114320.
[37] Kang D, Lee K, Kwon E, Tsuchiyama T, Takaki S. Variation of work hardening rate by oxygen contents in pure titanium alloy. Mater Sci Eng, A 2015;632:120–6. https://doi.org/10.1016/j.msea.2015.02.074.
[38] Li SJ, Jia MT, Prima F, Hao YL, Yang R. Improvements in nonlinear elasticity and strength by grain refinement in a titanium alloy with high oxygen content. Scripta Mater 2011;64:11. https://doi.org/10.1016/j.scriptamat.2011.02.006.
[39] Ngan AHW, Wen M. Dislocation kink-pair energetics and pencil glide in body-centered-cubic crystals. Phys Rev Lett 2001;87(7):075505. https://doi.org/10.1103/PhysRevLett.87.075505.
[40] Mahendran S, Carrez P, Cordier P. On the glide of [100] dislocation and the origin of 'pencil glide' in Mg_2SiO_4 olivine. Phil Mag 2019;99(22):2751–69. https://doi.org/10.1080/14786435.2019.1638530.
[41] Ben Haj Slama M, Maloufi N, Guyon J, Bahi S, Weiss L, Guitton A. In situ macroscopic tensile testing in SEM and electron channeling contrast imaging: pencil glide evidenced in a bulk β-Ti21S polycrystal. Materials 2019;12:15. https://doi.org/10.3390/ma12152479.
[42] Huang CX, Wang YF, Ma XL, Yin S, Höppel HW, Göken M, et al. Interface affected zone for optimal strength and ductility in heterogeneous laminate, Mater. Today Off 2018;21(7):713–9. https://doi.org/10.1016/j.mattod.2018.03.006.
[43] Yao T, Du K, Wang H, Qi L, He S, Hao Y, et al. Reversible twin boundary migration between α" martensites in a Ti-Nb-Zr-Sn alloy. Mater Sci Eng, A 2017;688:169–73. https://doi.org/10.1016/j.msea.2017.02.001.
[44] Yang Y, Castany P, Hao YL, Gloriant T. Plastic deformation via hierarchical nano-sized martensitic twinning in the metastable β Ti-24Nb-4Zr-8Sn alloy. Acta Mater 2020;194:27–39. https://doi.org/10.1016/j.actamat.2020.04.021.
[45] Dirras G, Ueda F, Hocini A, Tingaud D, Ameyama K. Cyclic shear behavior of conventional and harmonic structure-designed Ti-25Nb-25Zr β-titanium alloy: back-stress hardening and twinning inhibition. Scripta Mater 2017;138:44–7. https://doi.org/10.1016/j.scriptamat.2017.05.033.
[46] Bhattacharjee A, Bhargava S, Varma VK, Kamat SV, Gogia AK. Effect of β grain size on stress induced martensitic transformation in β solution treated Ti–10V–2Fe–3Al alloy. Scripta Mater 2005;53(2):195–200. https://doi.org/10.1016/j.scriptamat.2005.03.039.
[47] Chou K, Marquis EA. Oxygen effects on ω and α phase transformations in a metastable β Ti–Nb alloy. Acta Mater 2019;181:367–76. https://doi.org/10.1016/j.actamat.2019.09.049.
[48] Obbard EG, Hao YL, Talling RJ, Li SJ, Zhang YW, Dye D, et al. The effect of oxygen on α" martensite and superelasticity in Ti–24Nb–4Zr–8Sn. Acta Mater 2011;59:1. https://doi.org/10.1016/j.actamat.2010.09.015.
[49] Gubicza J. X-ray line profile analysis in materials science. IGI Global 2014. https://doi.org/10.4018/978-1-4666-5852-3.
[50] Zhang YW, Li SJ, Obbard EG, Wang H, Wang SC, Hao YL, et al. Elastic properties of Ti–24Nb–4Zr–8Sn single crystals with bcc crystal structure. Acta Mater 2011;59:8. https://doi.org/10.1016/j.actamat.2011.01.048.
[51] Dirras G, Gubicza J, Heczel A, Lilensten L, Couzinié JP, Perrière L, et al. Microstructural investigation of plastically deformed Ti20Zr20Hf20Nb20Ta20 high entropy alloy by X-ray diffraction and transmission electron microscopy. Mater Char 2015;108:1–7. https://doi.org/10.1016/j.matchar.2015.08.007.
[52] Hull D, Bacon D. Introduction to dislocations. Elsevier 2001. https://doi.org/10.1016/B978-0-7506-4681-9.X5000-7.
[53] Church NL, Hildyard EM, Jones NG. The influence of grain size on the onset of the superelastic transformation in Ti–24Nb–4Sn–8Zr (wt%). Mater Sci Eng, A 2021:142072. https://doi.org/10.1016/j.msea.2021.142072.
[54] Feaugas X. On the origin of the tensile flow stress in the stainless steel AISI 316L at 300 K: back stress and effective stress. Acta Mater 1999;47(13):3617–32. https://doi.org/10.1016/S1359-6454(99)00222-0.
[55] Zhu Y, Wu X. Heterostructured materials. Prog Mater Sci 2023;131:101019. https://doi.org/10.1016/j.pmatsci.2022.101019.